Magnetically Confined Wind Shocks on the Magnetic Massive Star θ^1Orionis C

Marc Gagné, Erin Shaughnessy, Hunter Mills (West Chester University),
Dinshaw Balsara, Sethupathy Subramanian (University of Notre Dame),
David Huenemoerder, Norbert Schulz (MIT Kavli Institute)

Credits: NASA, ESA, M. Robberto (Space Telescope Science Institute/ESA) and the Hubble Space Telescope Orion Treasury Project Team

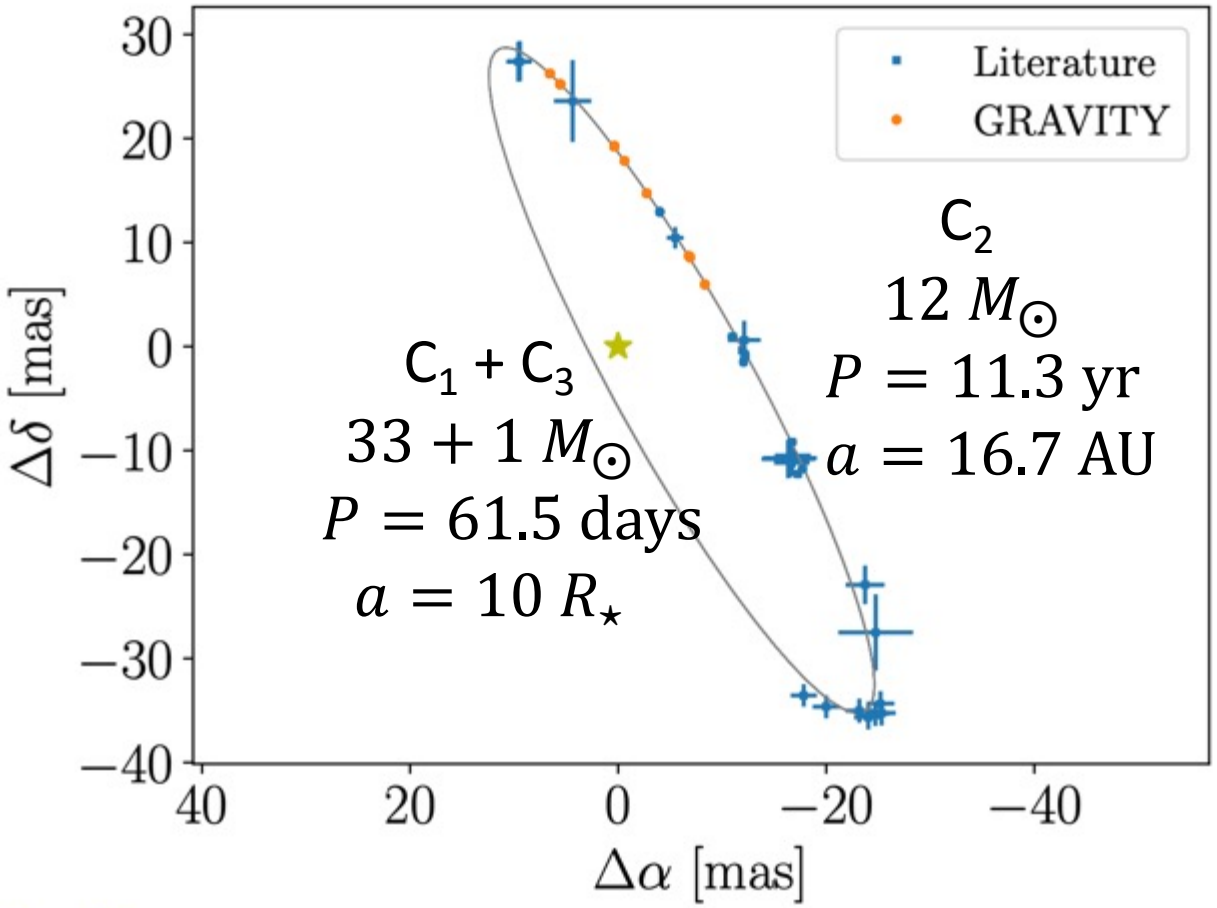

Fig. 7. Orbit of θ^1 Ori C_2. Orange dots are observed with GRAVITY, blue squares are positions taken from Weigelt et al. (1999), Schertl et al. (2003), Kraus et al. (2007, 2009), Patience et al. (2008), and Grellmann et al. (2013). The error bars of GRAVITY data are within the marker. The orbital parameters are listed in Table 1.

See also Rzaev et al. 2021.

Parameter	Symbol	Value
Mass	$M_\star$	33.4 $M_\odot$
Radius	$R_\star$	9.4 $R_\odot$
Luminosity	$L_\star$	2.0×10^5 $L_\odot$
Effective Temperature	T_{eff}	39000 K
CAK Mass loss rate	$\dot{M}_{B=0}$	1.2×10^{-7} $M_\odot$ yr^{-1}
Eddington parameter	Γ_e	0.16
CAK exponent	α	0.67
Q-factor	$\bar{Q}$	500
Terminal wind speed	V_∞	3200 km s^{-1}
Velocity exponent	β	0.8
Rotation rate	$\Omega_\star$	4.73×10^{-6} rad s^{-1}
Rotation parameter	W	0.041
Magnetic field strength at pole	B_p	1300 G
Magnetic tilt angle	ζ	45°
Magnetic confinement ratio	$\eta_\star$	75

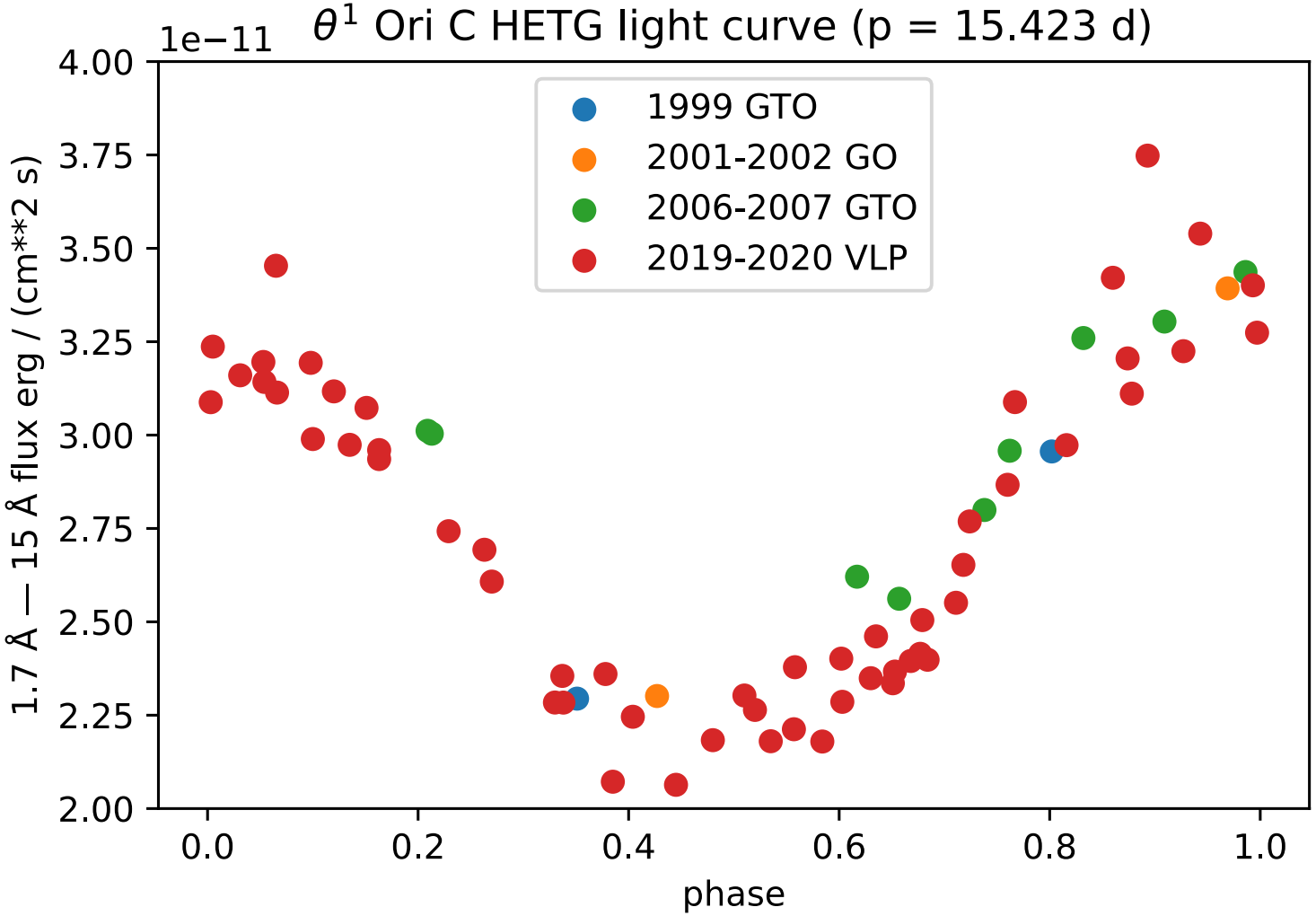

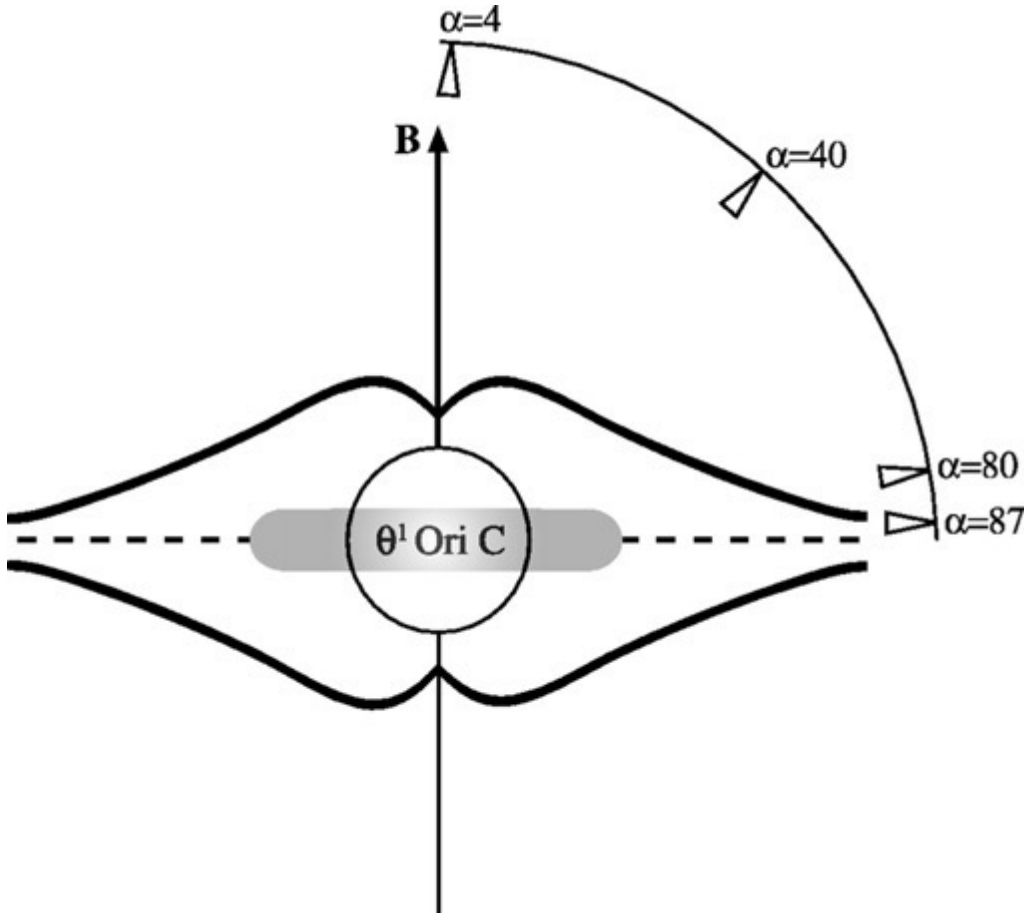

Left panel: Phase-folded *Chandra* HETG light curve of θ^1 Ori C, for a rotation period of 15.423 days. Grating spectra were obtained over 78 observations from 1999 to 2020. In the following figures, the observations were grouped into 11 phase bins to provide uniform signal-to-noise. *Right* panel: Schematic of θ^1 Ori C and its circumstellar environment (Gagné et al. 2005). The curved lines represent a set of magnetic field lines stretched out by the wind. The vector indicates the magnetic axis, and the dashed line represents the magnetic equatorial plane. The triangular arrows point to the observer at four different rotational phases. In this figure, taken from the perspective of the star's magnetic axis, the observer appears to move as a result of the magnetic obliquity, $\beta = 45°$. The rotation axis, which is inclined by 45° to the observer, is not shown because it too would move. The hard X-ray–emitting region is shown schematically as a gray torus. At high viewing angles, the entire torus is visible (X-ray maximum). At low viewing angles (X-ray minimum), some of the X-rays are occulted by the photosphere, and absorbed in the dense, cool wind within $2R_\star$.

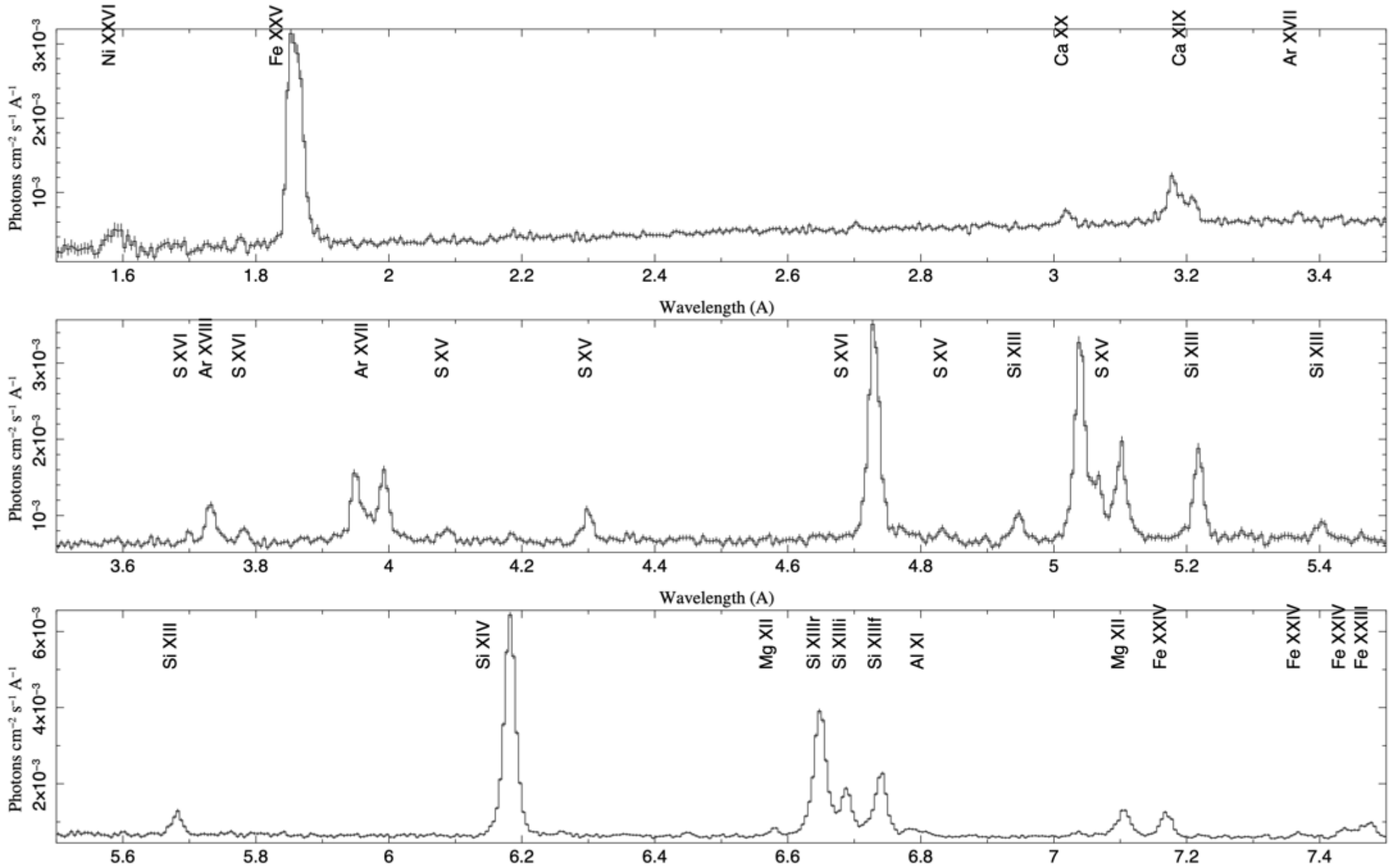
Ni XXVI
Fe XXV
Ca XX
Ca XIX
Ar XVII
Photons cm^{-2} s^{-1} A^{-1}
10^{-3}
2x10^{-3}
3x10^{-3}
1.6
1.8
2
2.2
2.4
2.6
2.8
3
3.2
3.4
Wavelength (A)
S XVI
Ar XVIII
S XVI
Ar XVII
S XV
S XV
S XVI
S XV
Si XIII
S XV
Si XIII
Si XIII
Photons cm^{-2} s^{-1} A^{-1}
10^{-3}
2x10^{-3}
3x10^{-3}
3.6
3.8
4
4.2
4.4
4.6
4.8
5
5.2
5.4
Wavelength (A)
Si XIII
Si XIV
Mg XII
Si XIIIr
Si XIIIi
Si XIIIf
Al XI
Mg XII
Fe XXIV
Fe XXIV
Fe XXIV
Fe XXIII
Photons cm^{-2} s^{-1} A^{-1}
2x10^{-3}
4x10^{-3}
6x10^{-3}
5.6
5.8
6
6.2
6.4
6.6
6.8
7
7.2
7.4

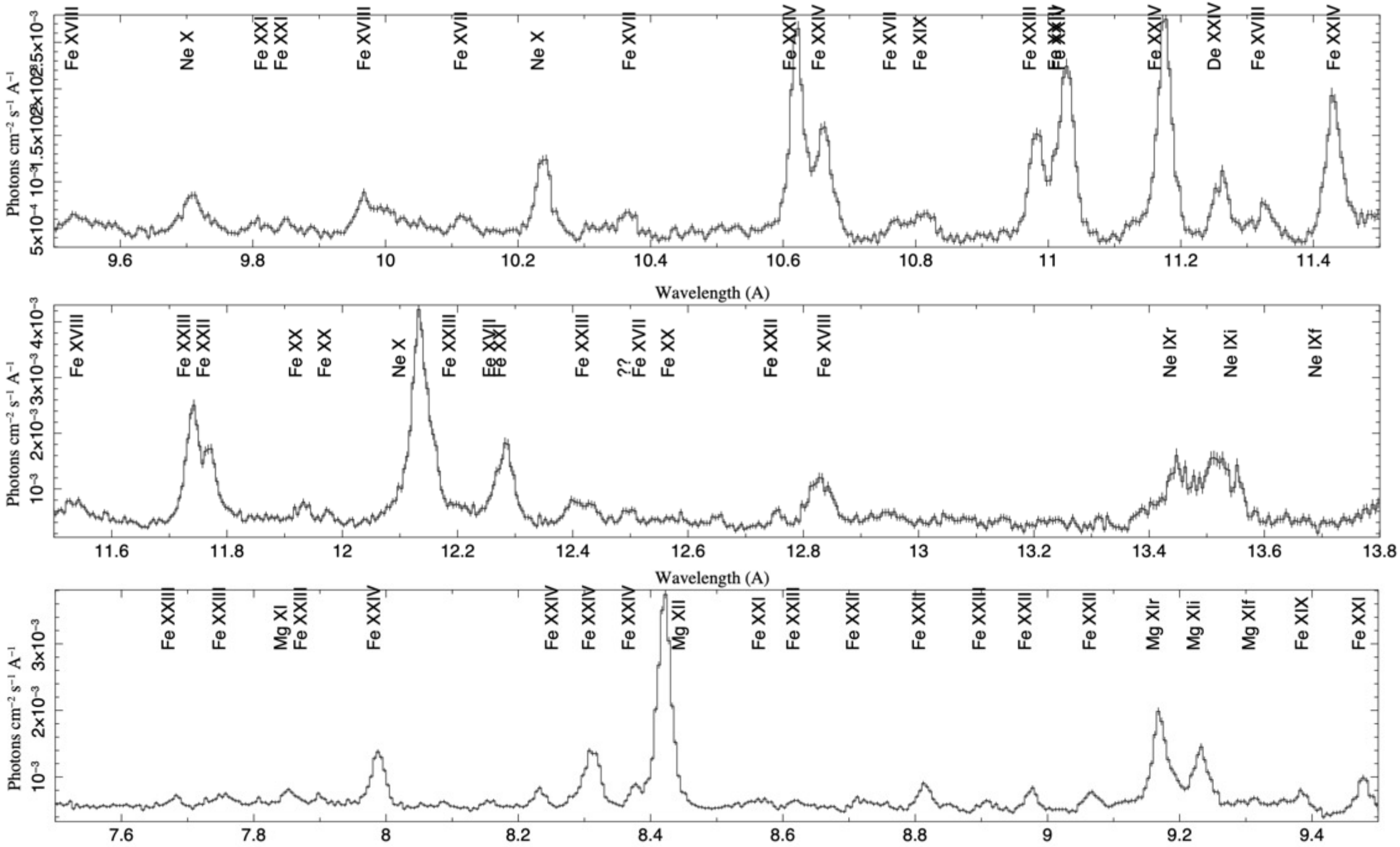
Photons cm^{-2} s^{-1} A^{-1}
Wavelength (A)
Fe XVIII
Ne X
Fe XXI
Fe XXI
Fe XVIII
Fe XVII
Ne X
Fe XVII
Fe XXIV
Fe XXIV
Fe XVII
Fe XIX
Fe XXIII
Fe XXIV
Fe XXIV
De XXIV
Fe XVIII
Fe XXIV
Fe XVIII
Fe XXIII
Fe XXII
Fe XX
Fe XX
Ne X
Fe XXIII
Fe XXII
Fe XXIII
?? Fe XVII
Fe XX
Fe XXII
Fe XVIII
Ne IXr
Ne IXi
Ne IXf
Fe XXIII
Fe XXIII
Mg XI
Fe XXIII
Fe XXIV
Fe XXIV
Fe XXIV
Fe XXIV
Mg XII
Fe XXI
Fe XXIII
Fe XXII
Fe XXII
Fe XXIII
Fe XXII
Fe XXII
Mg XIr
Mg XIi
Mg XIf
Fe XIX
Fe XXI

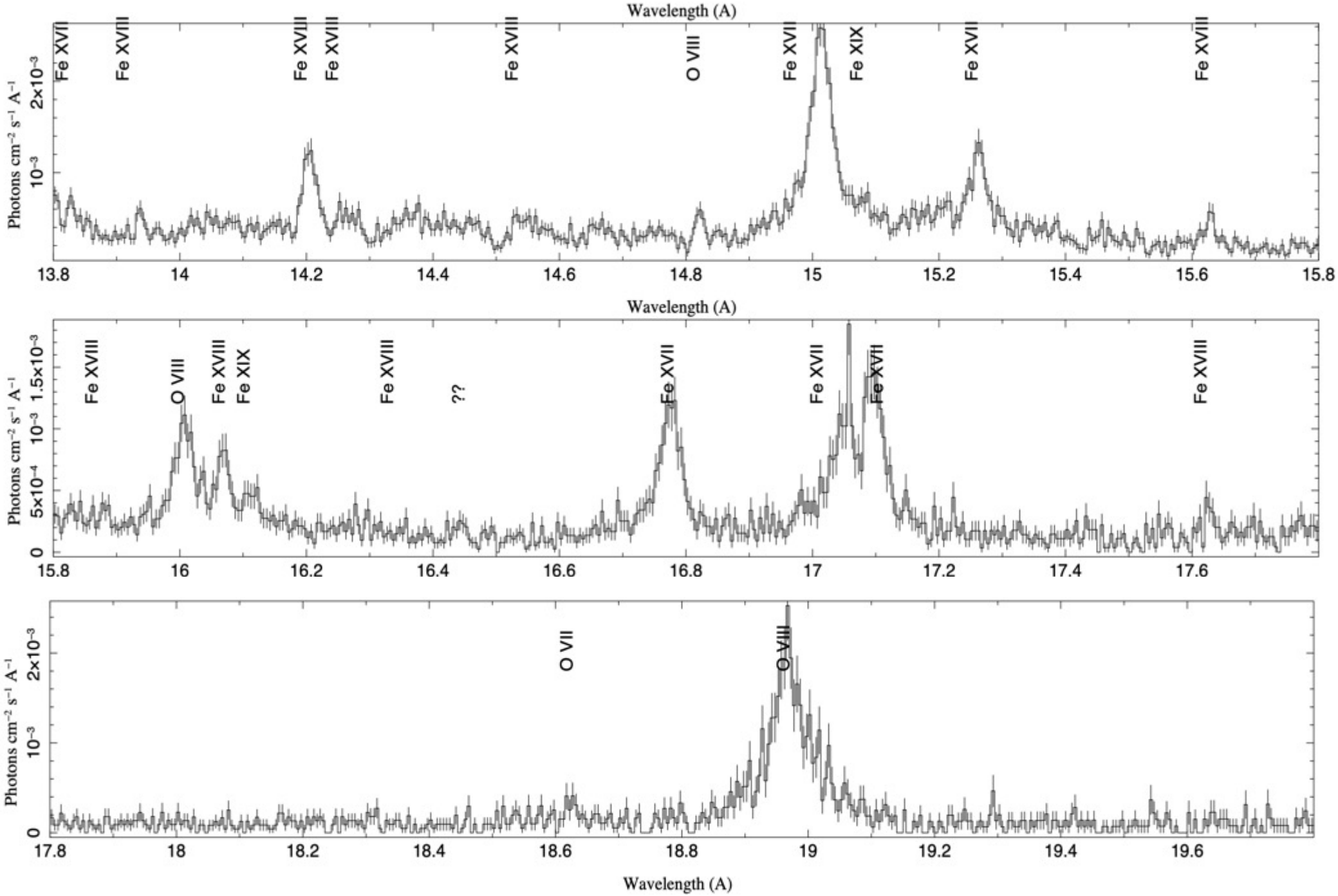
Wavelength (A)
Photons cm^{-2} s^{-1} A^{-1}
Fe XVII
Fe XVIII
Fe XVIII
Fe XVIII
Fe XVIII
O VIII
Fe XVII
Fe XIX
Fe XVII
Fe XVIII
Fe XVIII
O VIII
Fe XVIII
Fe XIX
Fe XVIII
??
Fe XVII
Fe XVII
Fe XVII
Fe XVIII
O VII
O VIII
Wavelength (A)

HETG Fitting Procedures

- 78 sets of HEG/MEG spectra were coadded and fit in ISIS
  - 11 phase-binned HEG/MEG line fits
  - Total 2.1 Ms line fits

- For each set, 6T variable abundance APEC model (very close to solar abundance)

- For each set, each line complex was fit two ways:
  - All lines + continuum only
  - Key line(s) + (6T APEC model – key line(s))
  - Voigt profiles: Gaussian + Lorentzian

- Aims:
  - To accurately measure key line fluxes, widths, and shifts.
  - To properly account for continuum and satellite line emission

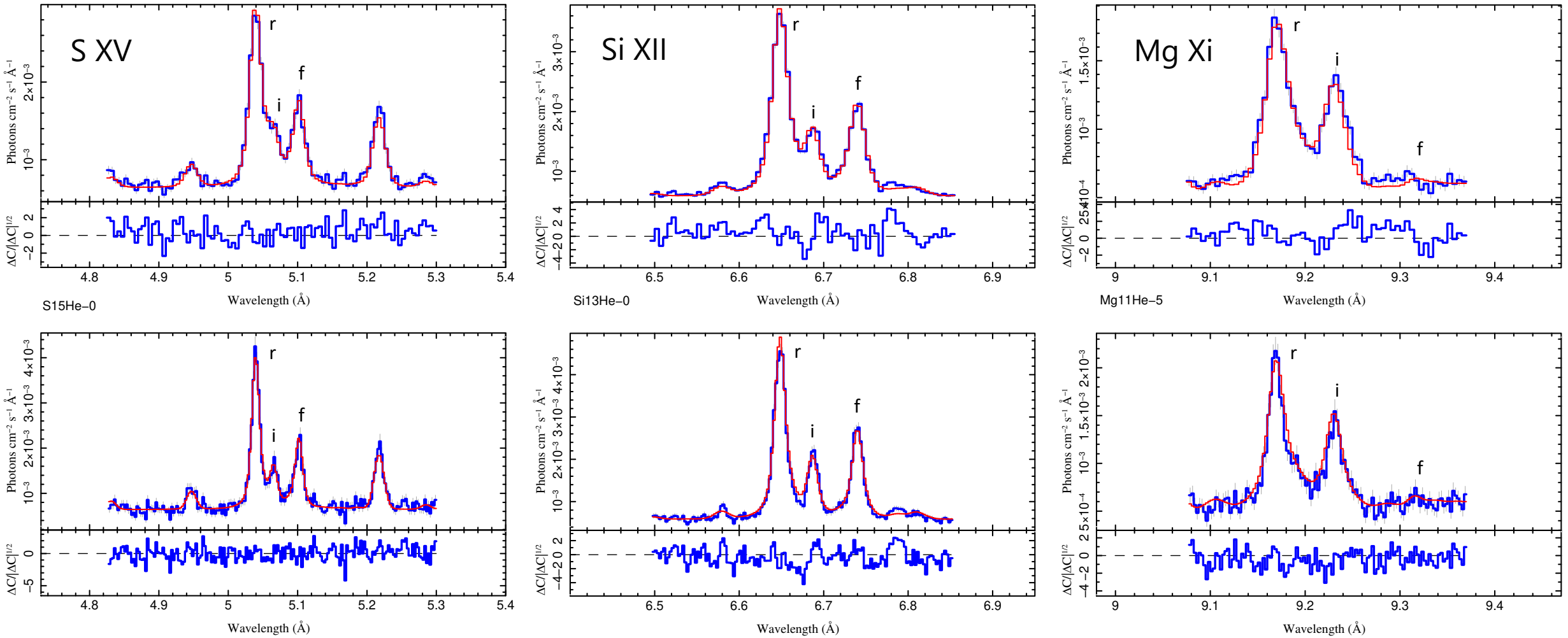

MEG (top) and HEG (bottom) spectra (blue) and model (red) of the resonance (r), intercombination (i) and forbidden line complexes of the He-like ions: S XV (left panels), Si XIII (middle panels), and Mg XI (right panels). Note that the forbidden-to-intercombination line ratio $\mathcal{R} = \frac{f}{i}$ decreases significantly from left to right. The $\mathcal{R}$ ratio of each ion is sensitive to far-UV photoexcitation. The $G = \frac{f+i}{r}$ ratio is sensitive to plasma temperature.

HETG Fitting Results

- All lines require a non-thermal Voigt profile, larger Lorentzian component

- All hot lines from Fe XXV to Mg XII show:
  - similar 40% variability
  - ~400 km/s FWHM
  - No line shifts
  - Formed in X-ray torus at $2 - 3\ R_\star$

- Cooler lines of Fe XVII and O VIII show:
  - No systemic variability
  - ~1,000 km/s FWHM
  - No line shifts
  - Formed in outlflow beyond $2\ R_\star$

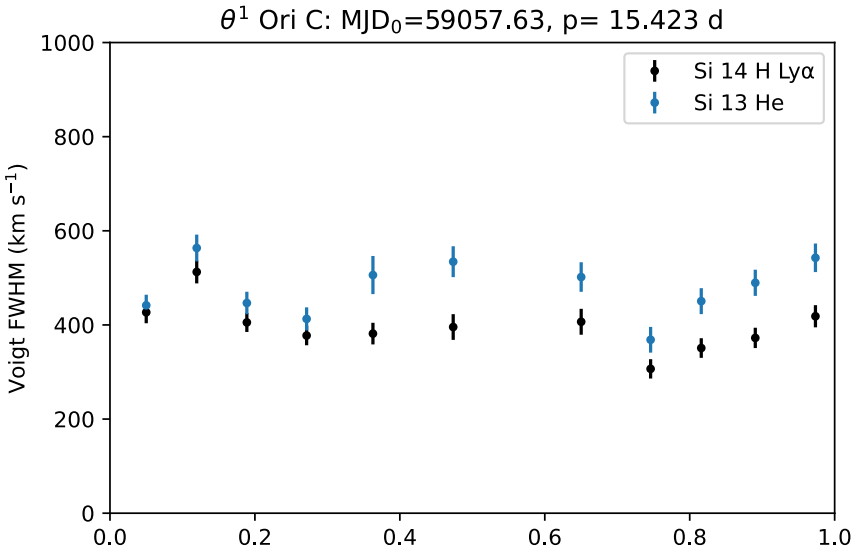

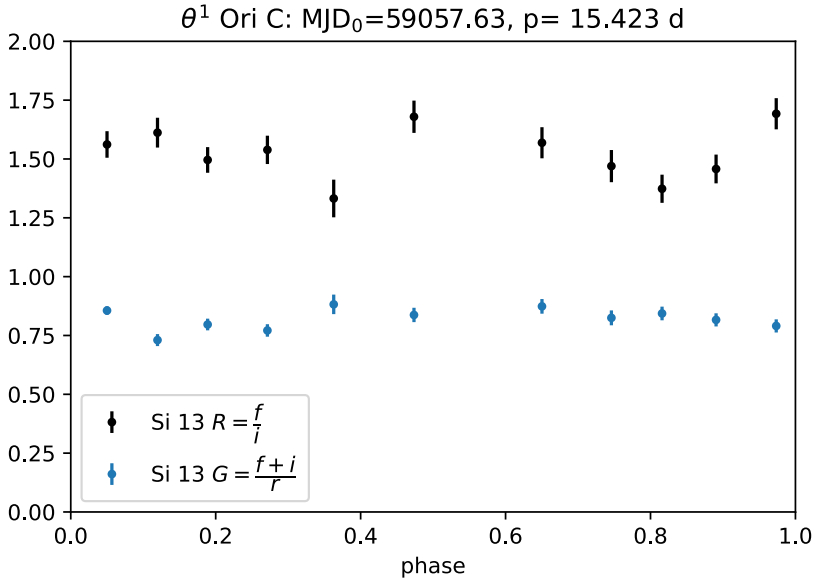

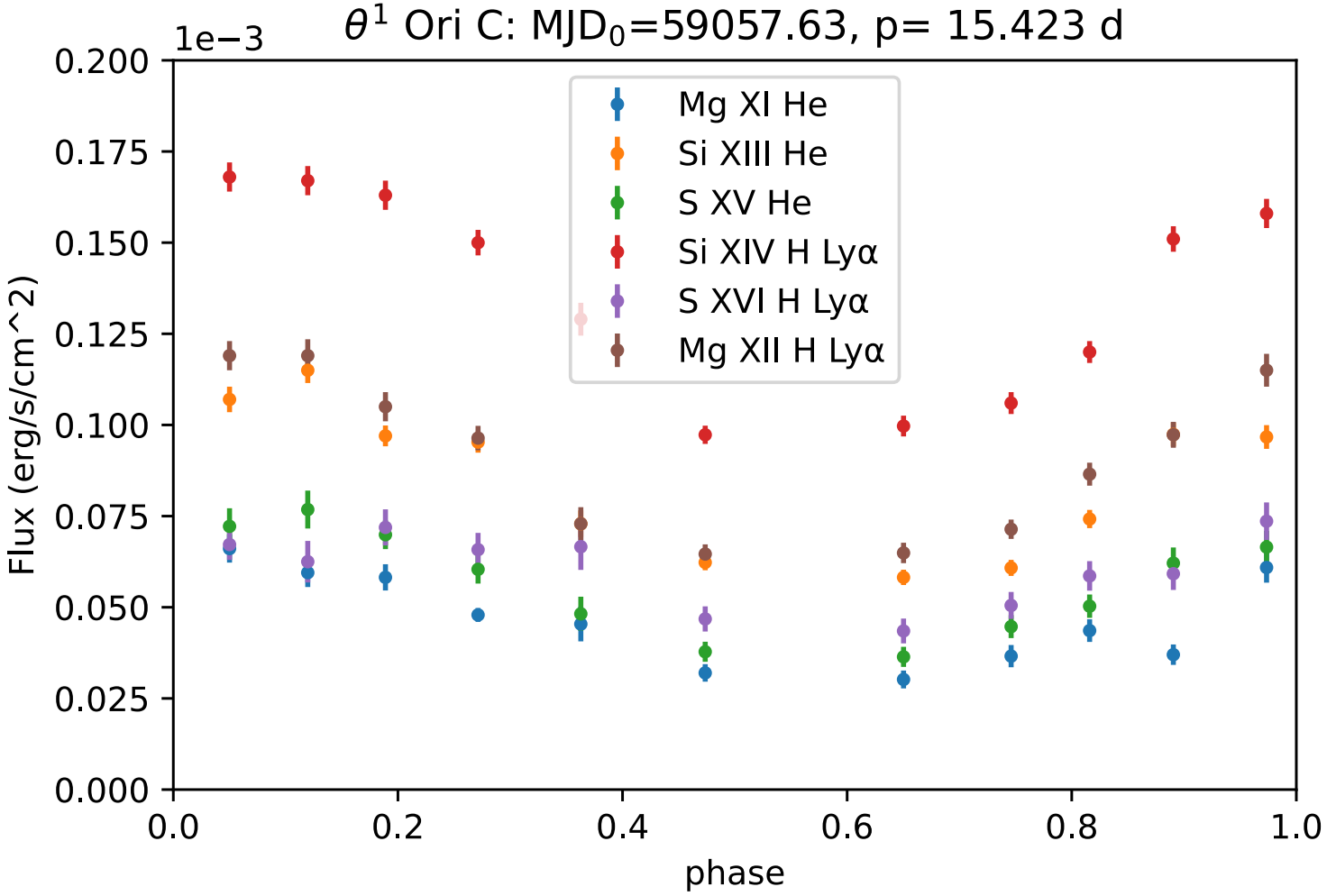

Top left: The emission lines have non-thermal line widths ranging from 300-500 km/s in the hottest lines (e.g., Si XIV and SXVI) to 1000 km/s for the coolest lines (e.g., O VIII, Fe XVII, not shown). The lines also show phase-dependent line width variations. *Lower left*: The temperature-sensitive G ratios show no significant phase variations, but the R ratios do. R is sensitive to photoexcitation, and hence to the location of the X-ray shocks relative to the FUV bright photosphere. *Right*: Individual line fluxes show a consistent 40-45% drop in flux from X-ray maximum to minimum.

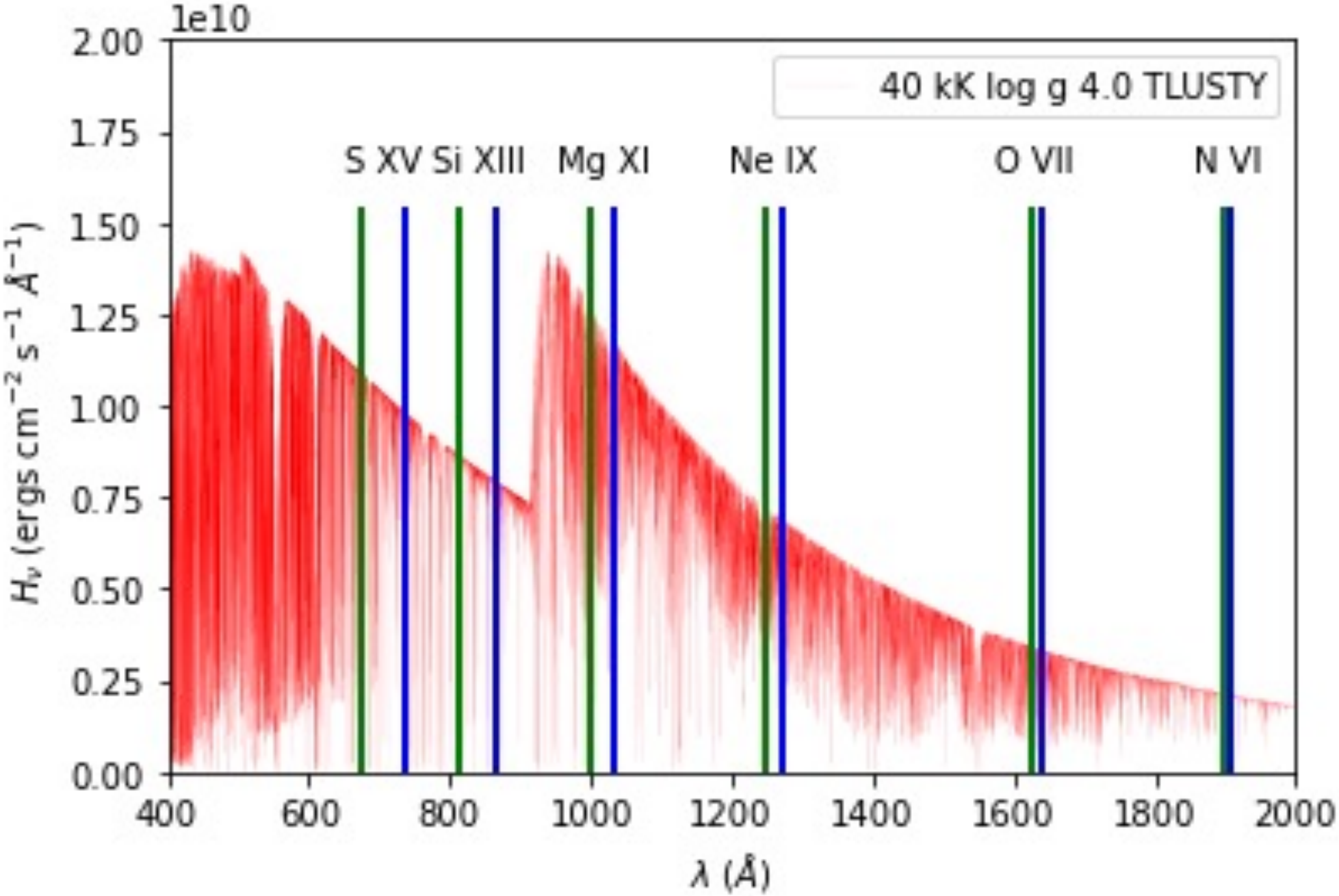
1e10
2.00
1.75
1.50
1.25
1.00
0.75
0.50
0.25
0.00
40 kK log g 4.0 TLUSTY
S XV
Si XIII
Mg XI
Ne IX
O VII
N VI
H_ν (ergs cm^{-2} s^{-1} Å^{-1})
400
600
800
1000
1200
1400
1600
1800
2000
λ (Å)

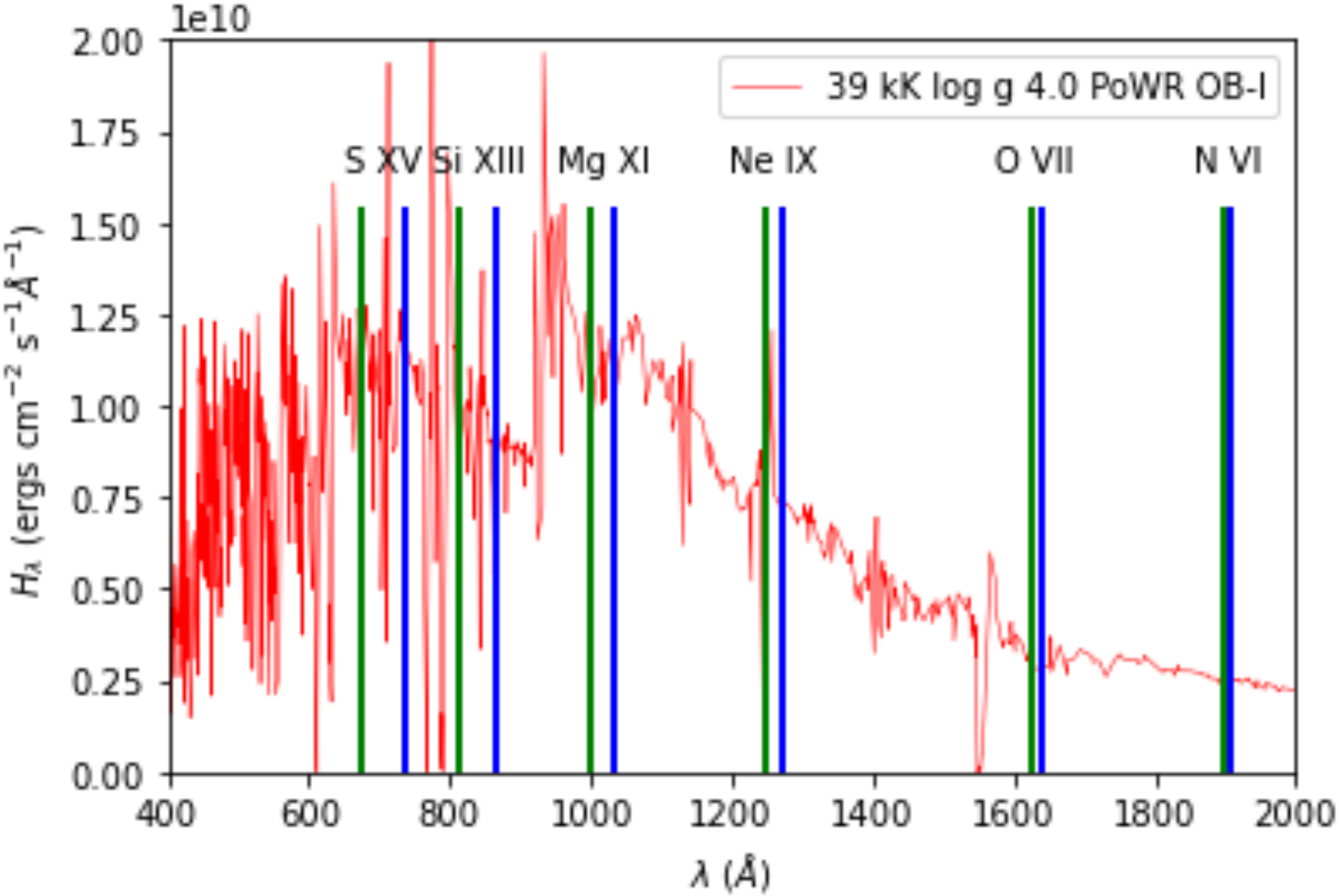
1e10
2.00
1.75
1.50
1.25
1.00
0.75
0.50
0.25
0.00
H_λ (ergs cm^{-2} s^{-1}Å^{-1})
39 kK log g 4.0 PoWR OB-I
S XV
Si XIII
Mg XI
Ne IX
O VII
N VI
400
600
800
1000
1200
1400
1600
1800
2000
λ (Å)

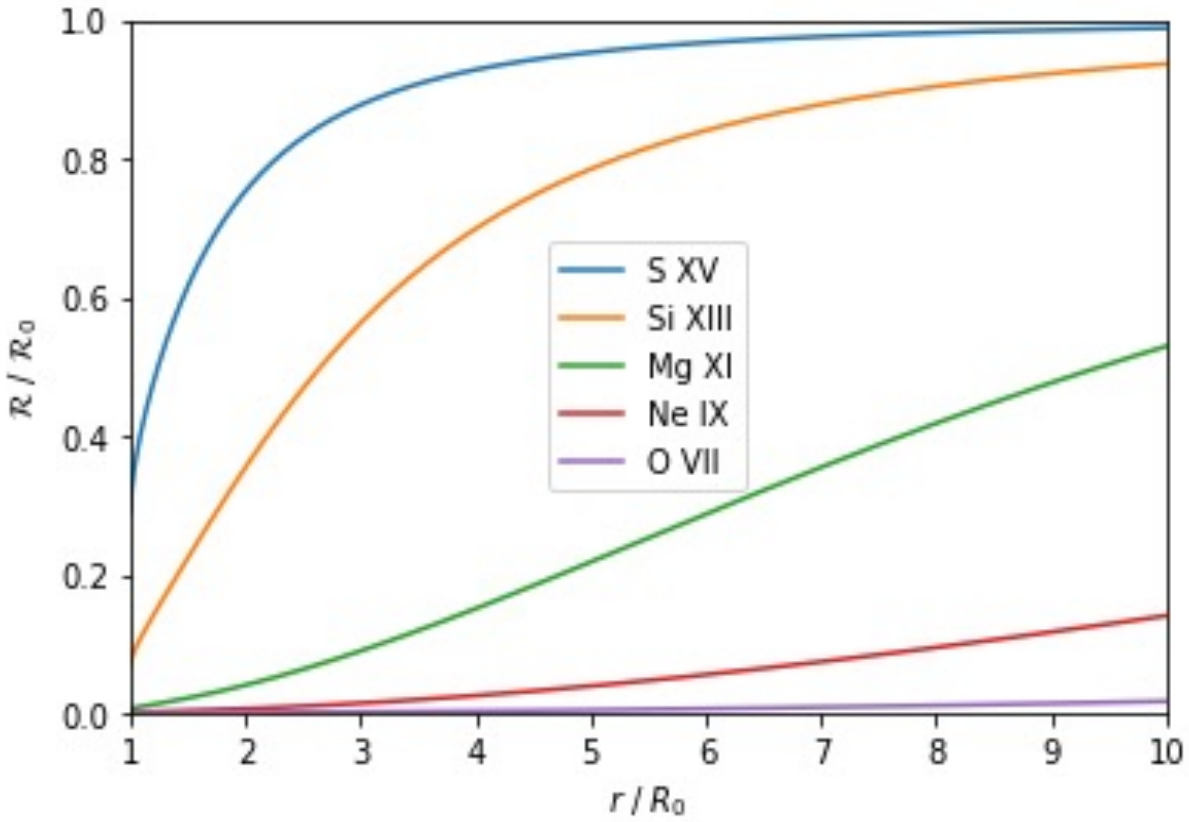

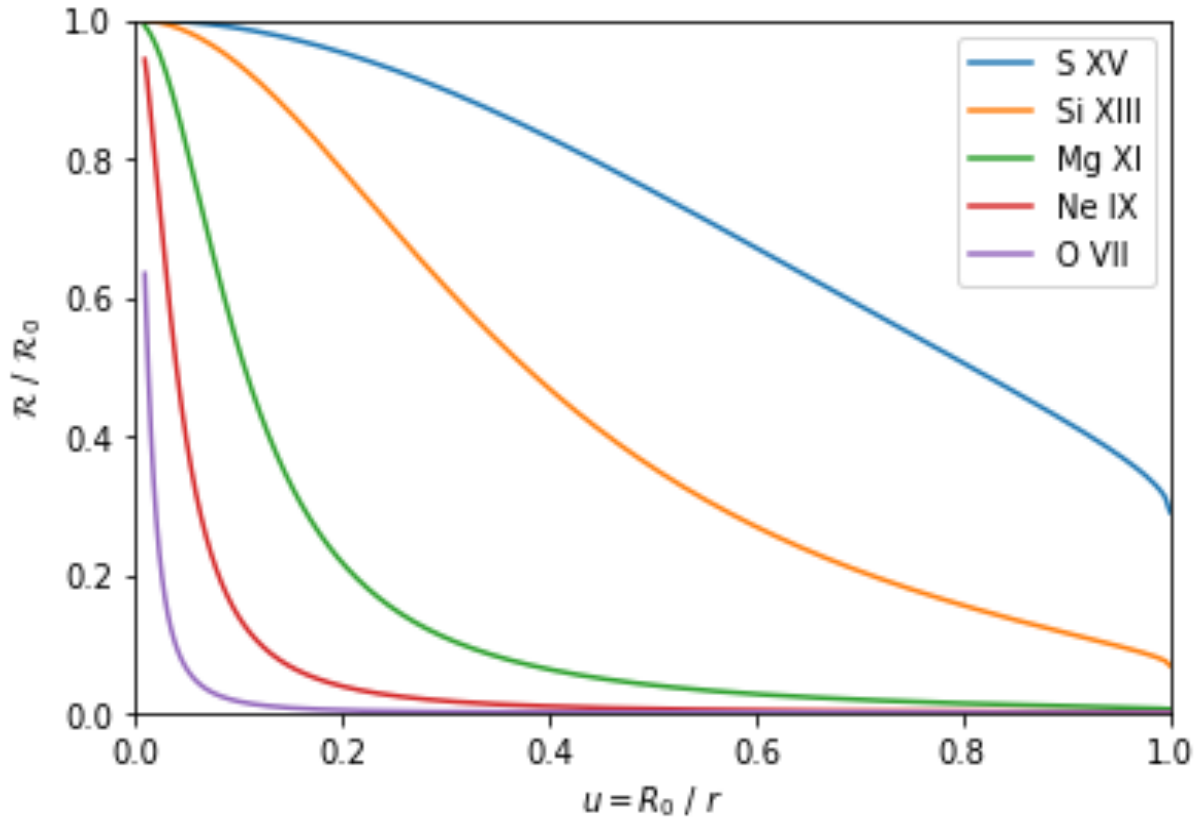

Model forbidden-to-intercombination line ratio $\mathcal{R} = \frac{f}{i}$, normalized to the zero-flux ratio $\mathcal{R}_0$, as a function of stellar radius $r/R_\star$(left) and inverse radial coordinate $u = R_\star/r$, using the TLUSTY 40kK SED flux and the formalism of Leutenegger et al. (2006), for five He-like ions.

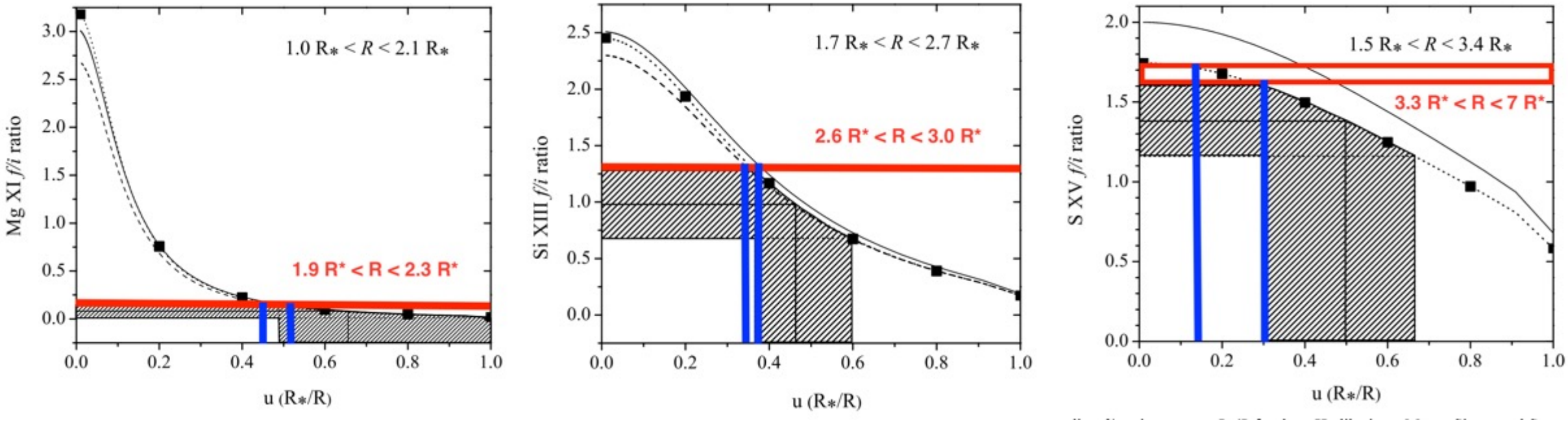

FIG. 13.—Forbidden-to-intercombination line f/i ratios vs. $u = R_\star/R$ for three He-like ions: Mg XI, Si XIII, and S XV, assuming a photospheric temperature $T_{\rm eff} =$ 40,000 K. The hatched regions represent the 1 σ upper and lower bounds on the observed f/i ratios and the corresponding bounds on $u = R_\star/R$ from the PRISMSPECT model (*dotted line and filled squares*), G. R. Blumenthal et al. (ApJ, 172, 205 [1972]; *solid line*), and D. Porquet et al. (A&A, 376, 1113 [2001]; *dashed line*).

Preliminary $\mathcal{R}$ ratio analysis

The measured $\mathcal{R}$ ratios (and 1σ errors) for Mg XI, Si XIII and S XV are represented by the horizontal red lines. The corresponding limits on the inverse radial coordinate $u = R_\star/r$ are shown as vertical blue lines, and the resulting limits on R are indicated in red. These results are overplotted on the results of Gagné et al. (2005) in black, for the 40 kK TLUSTY SED.

Three Key Parameters Regulate Mass Loss and Angular Momentum Loss in Massive Magnetized Star Winds

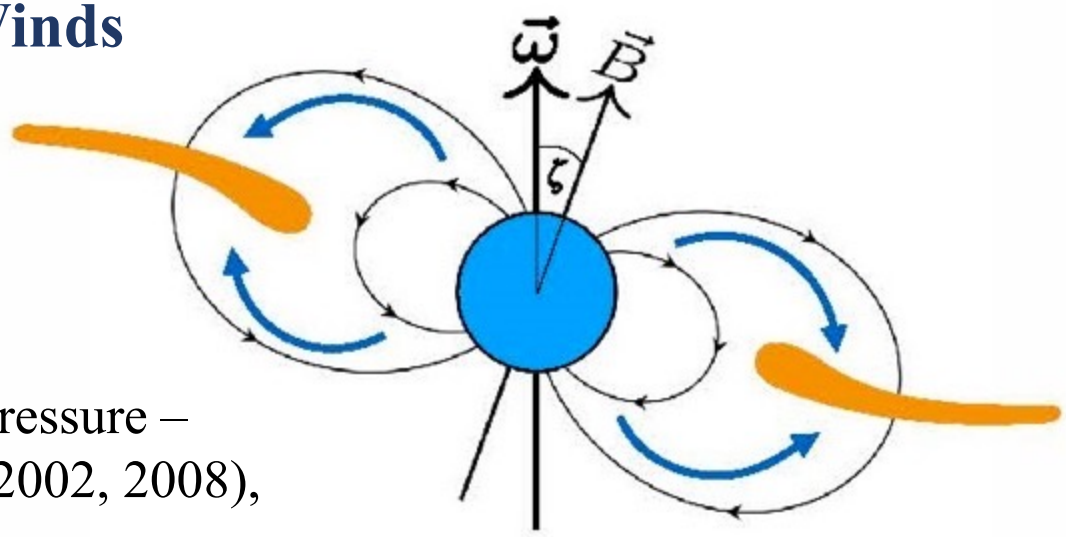

1. Competition between magnetic pressure and wind ram pressure – Wind magnetic confinement parameter (ud-Doula *et al*. 2002, 2008),

$$\eta_* = \frac{B_*^2\ R_*^2}{\dot{M}\ V_\infty} \quad \Rightarrow \quad R_A \approx R_* \left[0.3 + \left(\eta_* + 0.25 \right)^{1/4} \right] \quad \leftarrow \text{ Magnetic field releases its clutches on gas at Alfven radius.}$$

2. Ratio of rotational speed to orbital speed:-

$$W = \frac{V_{rot}}{V_{orb}} = \frac{\omega\ R_*}{\sqrt{GM_*/R_*}} \quad \Rightarrow \quad R_K = W^{-2/3} R_* \quad \leftarrow \text{ Rotational forces become important past this radius}$$

3. The angle ζ between rotation axis and magnetic dipole.

Meshing the Sphere

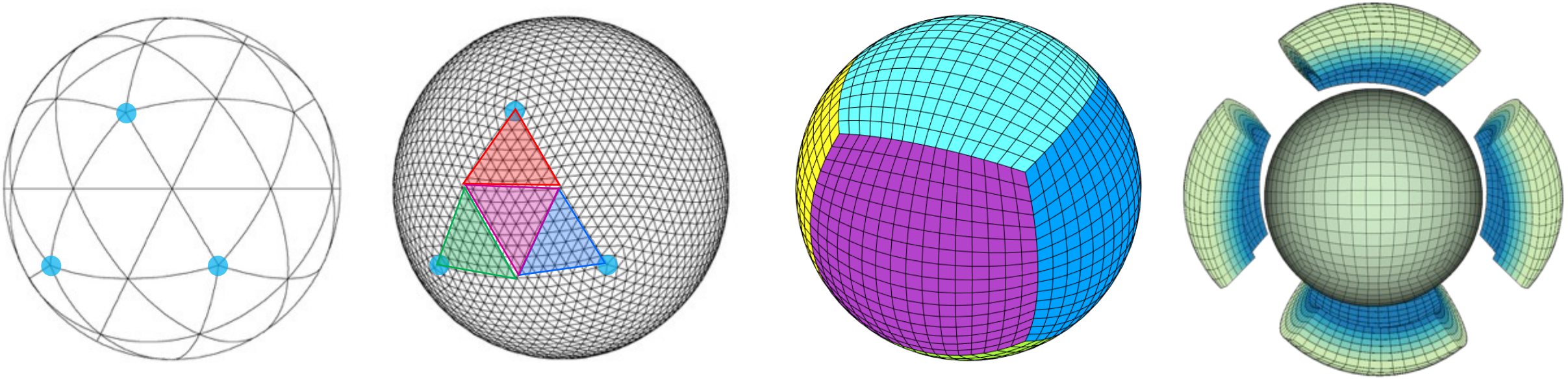

Left two panels: Version 1 of the Riemann Geomesh code used an icosahedral geodesic mesh to map the sphere with 20 triangular sectors. Right two panels: Version 2 of the code uses a Cubesphere to map the sphere with 6 fundamental square sectors. In either case, each sector is subdivided 2^{2n} times. In both cases, the sphere is extruded radially using a logarithmic radial mesh from $1 - 7R_{\star}$.

3D MHD with full energy equation

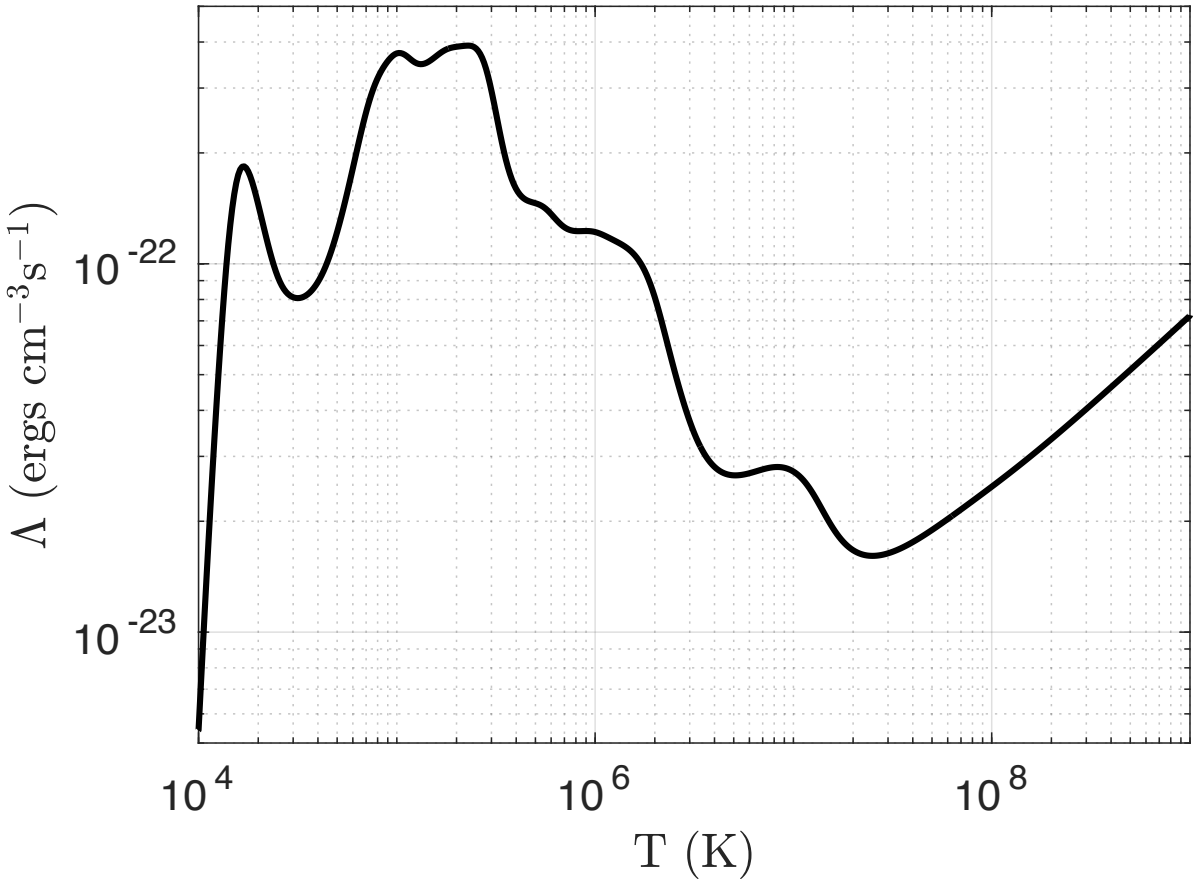

Riemann Geomesh features:

- CAK source function
- Tilted, rotating magnetic dipole
- Shock heating
- Radiative cooling (solar abundance, CHIANTI cooling function)
- Inverse-Compton cooling

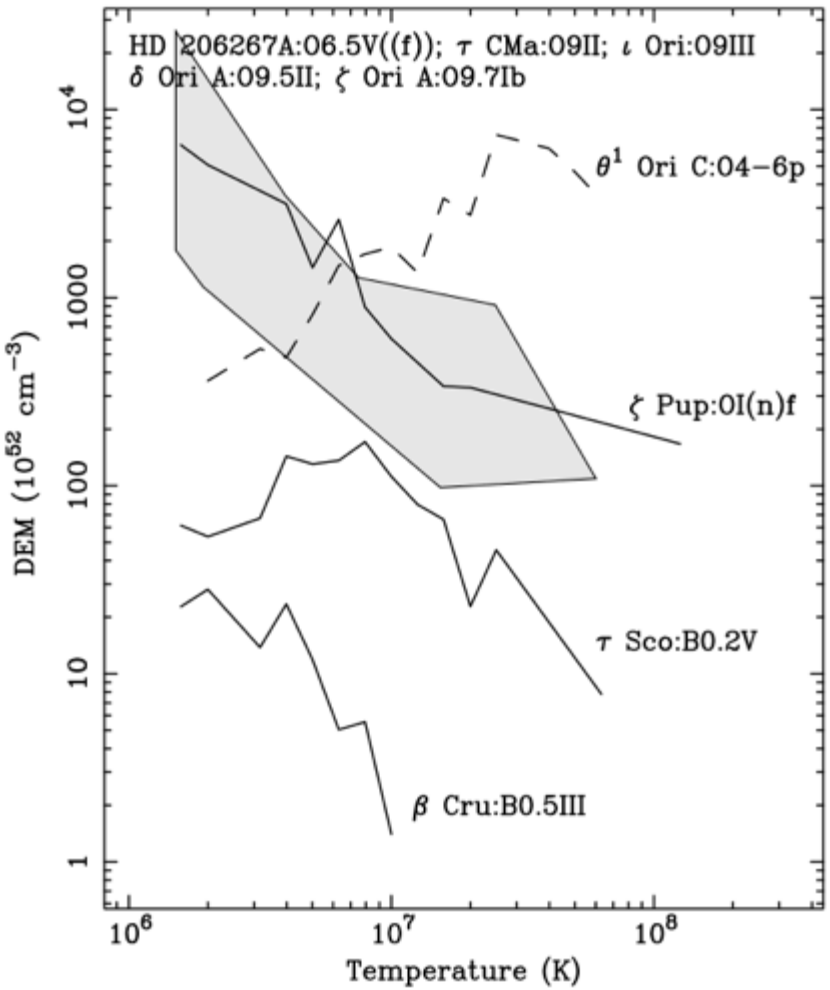

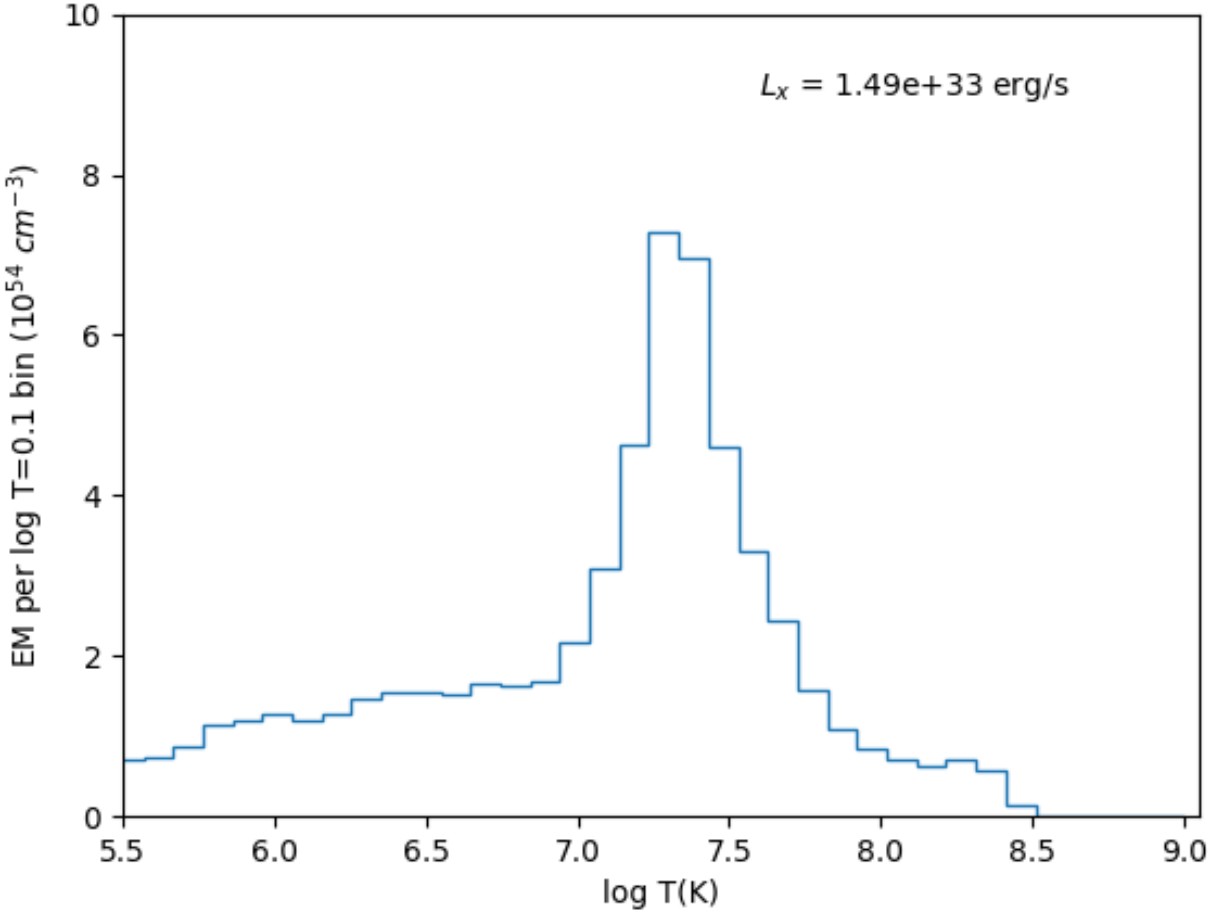

Left: EM distributions for two magnetic (θ^1 Ori C and τ Sco) and two non-magnetic OB stars (Wojdowski & Schulz 2005). *Right*: The θ^1 Ori C simulation shows a broad emission-measure distribution, with a peak near log $T = 7.4$, and an unabsorbed X-ray luminosity $L_X \approx 1.5{\times}10^{33}$ erg s^{-1}, consistent with the spectral data analysis.

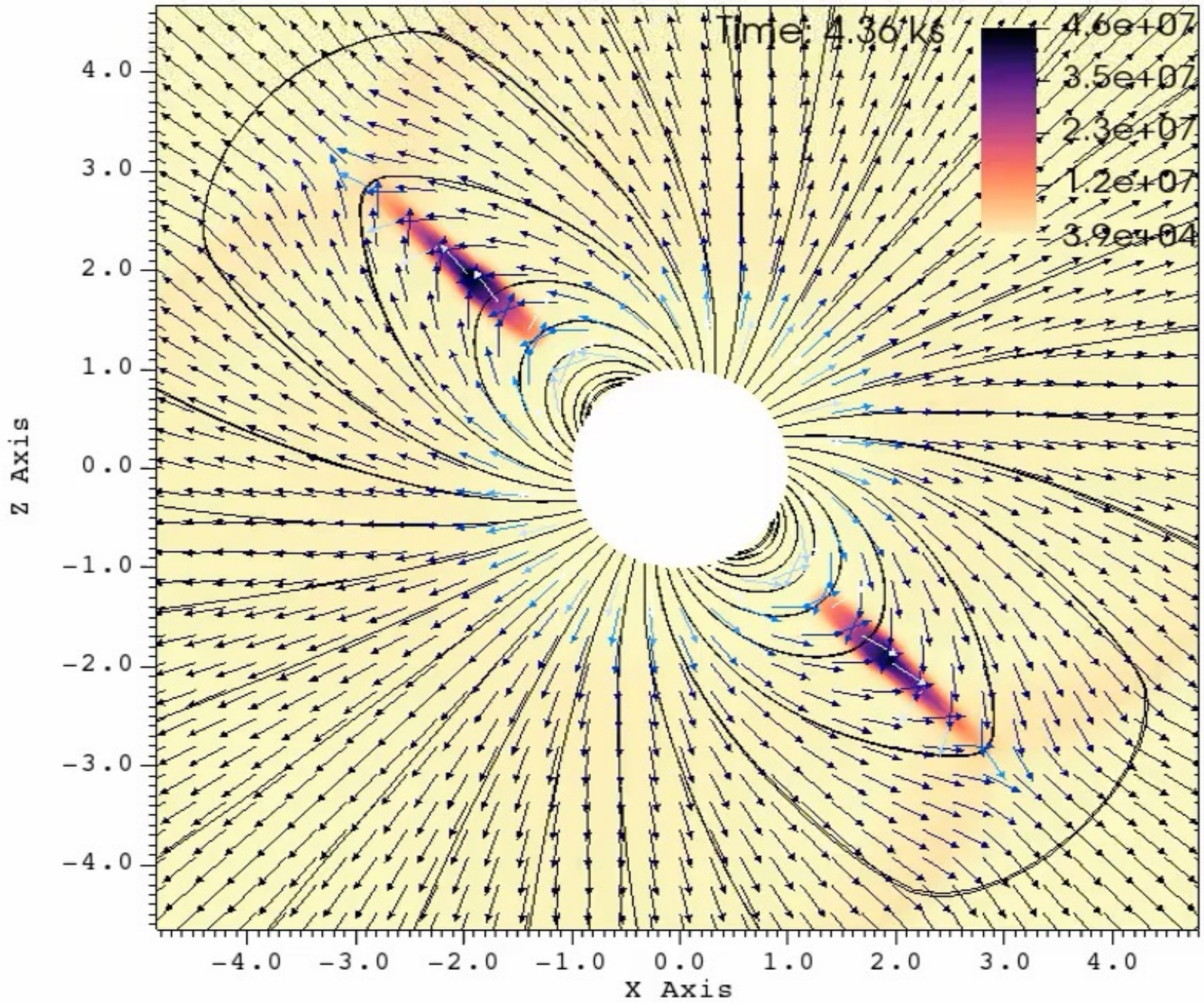
Time: 4.36 ks
4.6e+07
3.5e+07
2.3e+07
1.2e+07
3.9e+04
Z Axis
X Axis
4.0
3.0
2.0
1.0
0.0
-1.0
-2.0
-3.0
-4.0
-4.0
-3.0
-2.0
-1.0
0.0
1.0
2.0
3.0
4.0

Sim-A: Evolution of Density, Temperature (colorized) with Magnetic field lines

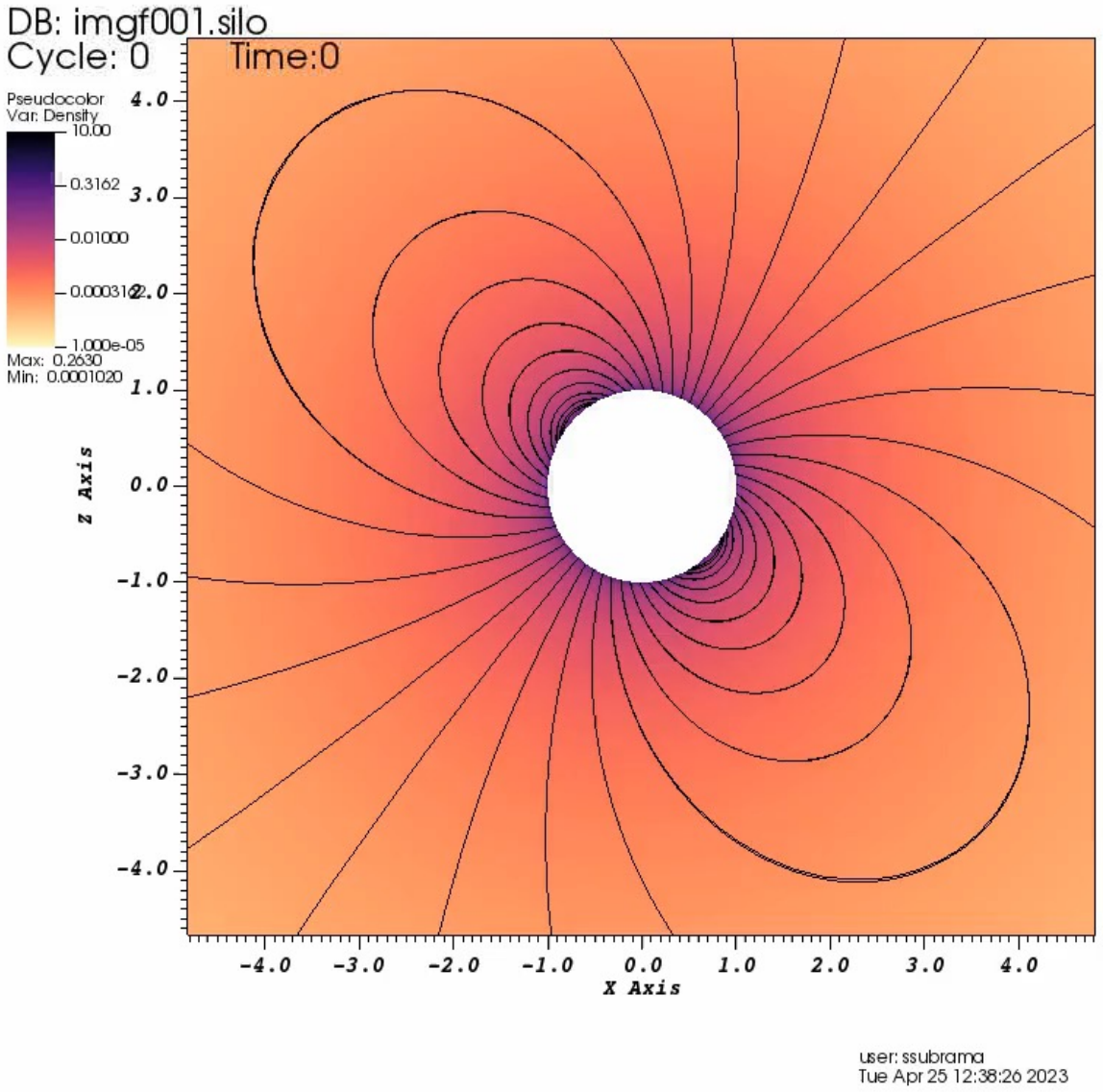

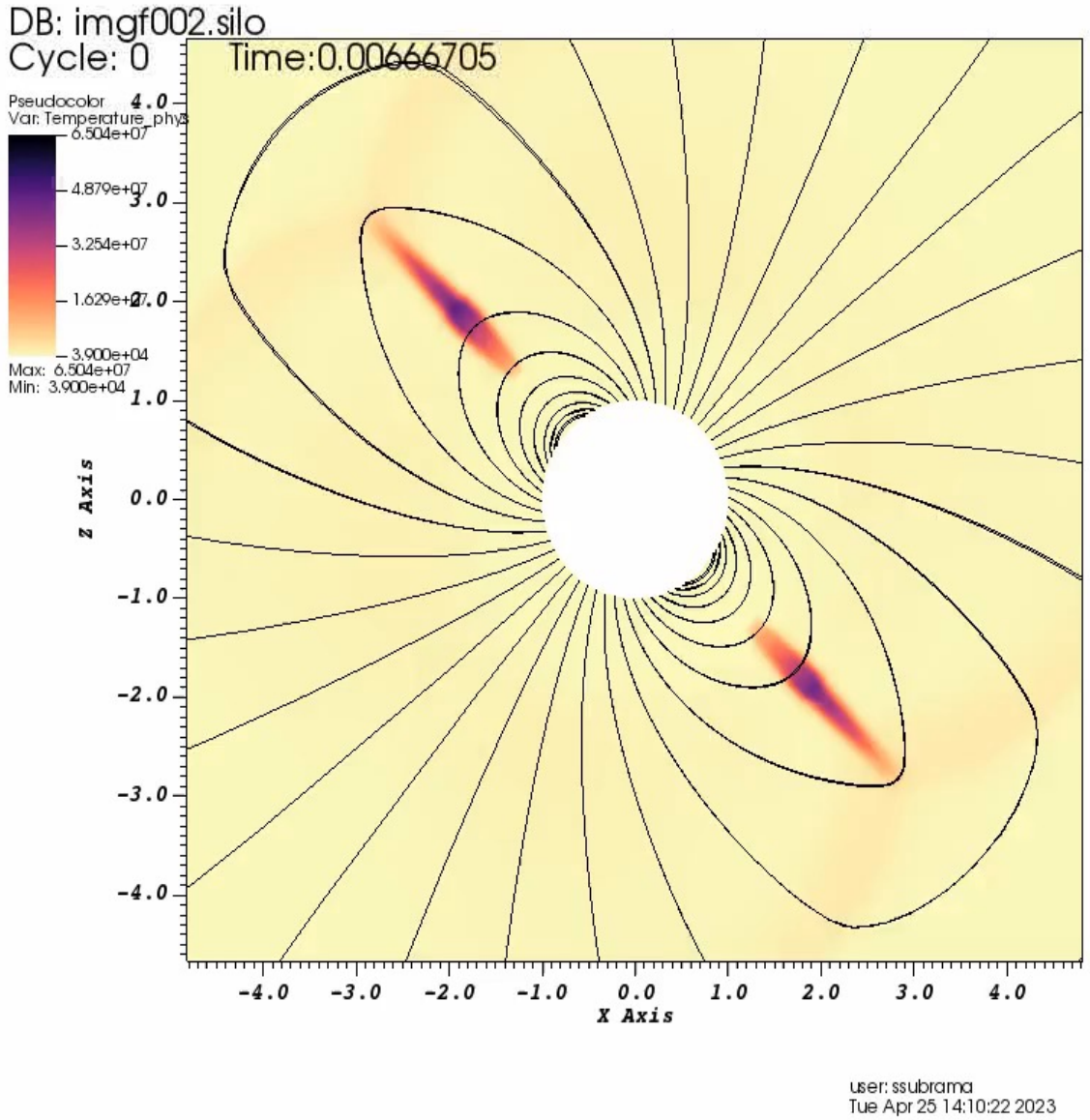

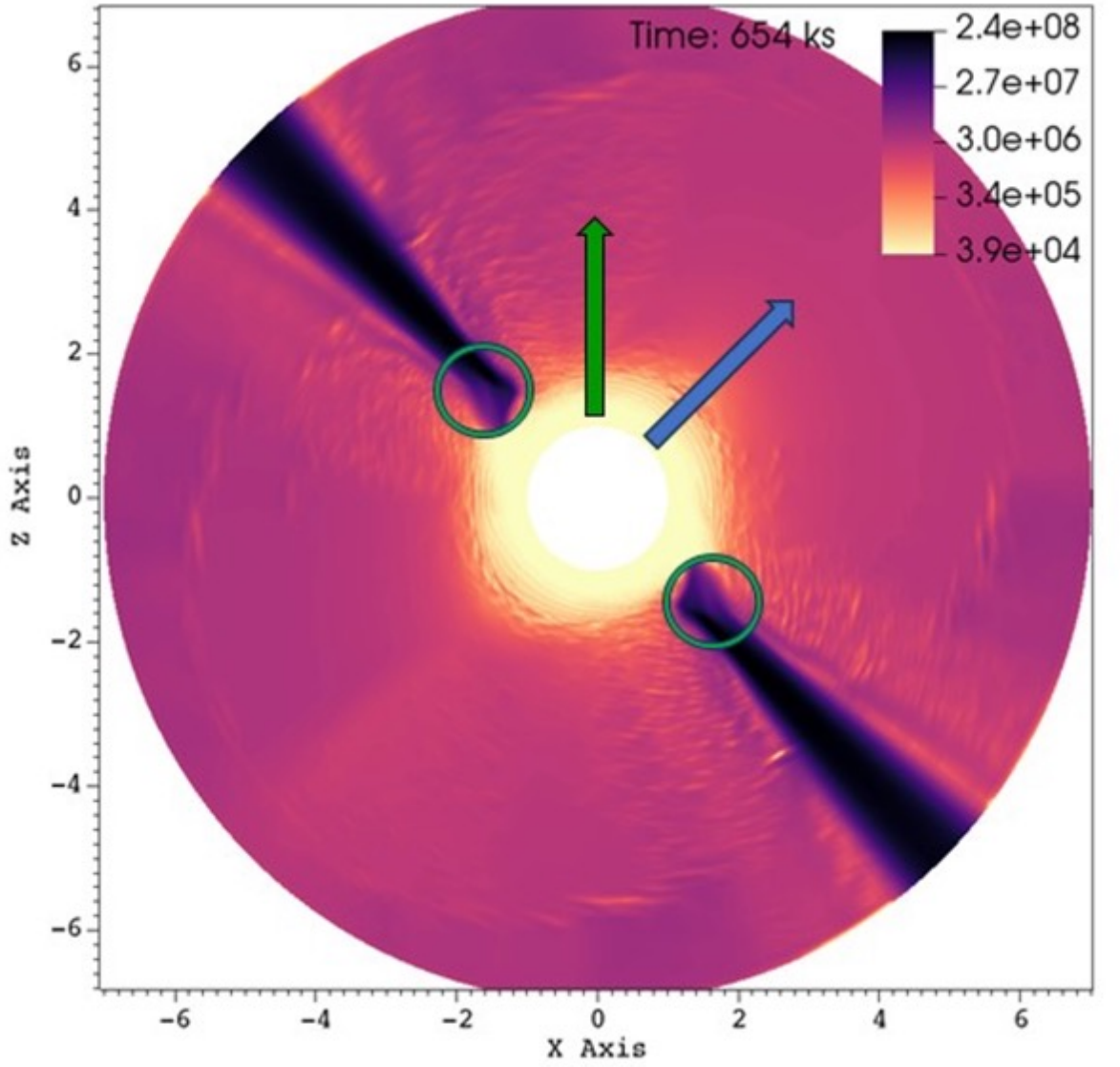

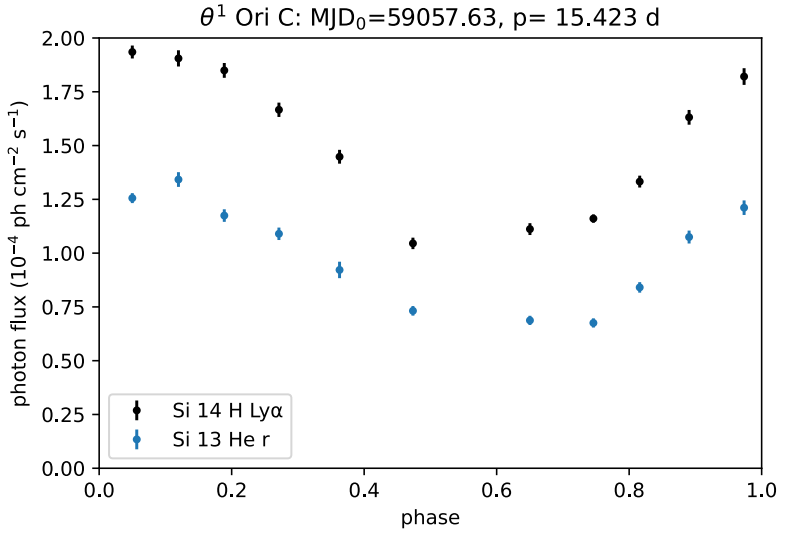

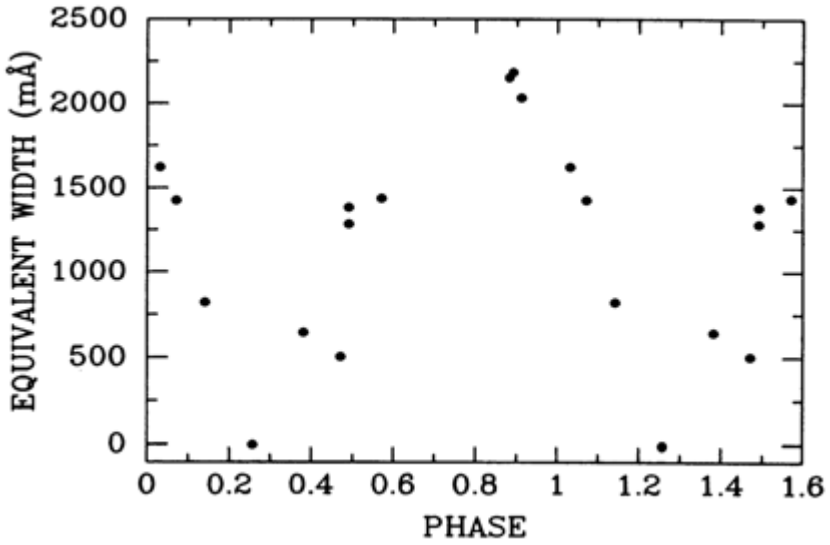

Left panel: Log temperature slice in the XZ plane. The rotation axis is shown in green; the magnetic axis is shown in blue. At X-ray maximum (phase 0.0), the observer is looking down the magnetic axis. At X-ray minimum (phase 0.5) the observer is looking down the hot X-ray disc, perpendicular to the magnetic axis. The very hot plasma with the highest density and emission measure is circled in green at $\sim 2R_\star$. The cooler, denser gas below 10^5 K (in yellow) has a much higher cross-section for X-ray photo-electric absorption. The 3D simulation confirms both the X-ray variations (in the *upper right* panel) and the excess C IV absorption (in the *lower right* panel, Fig. 3 from Walborn & Nichols 1994). The excess absorption seen in the blue wing of C IV along the magnetic axis may be caused by the outflowing yellow/orange plasma below $\sim 5\times 10^5$ K.

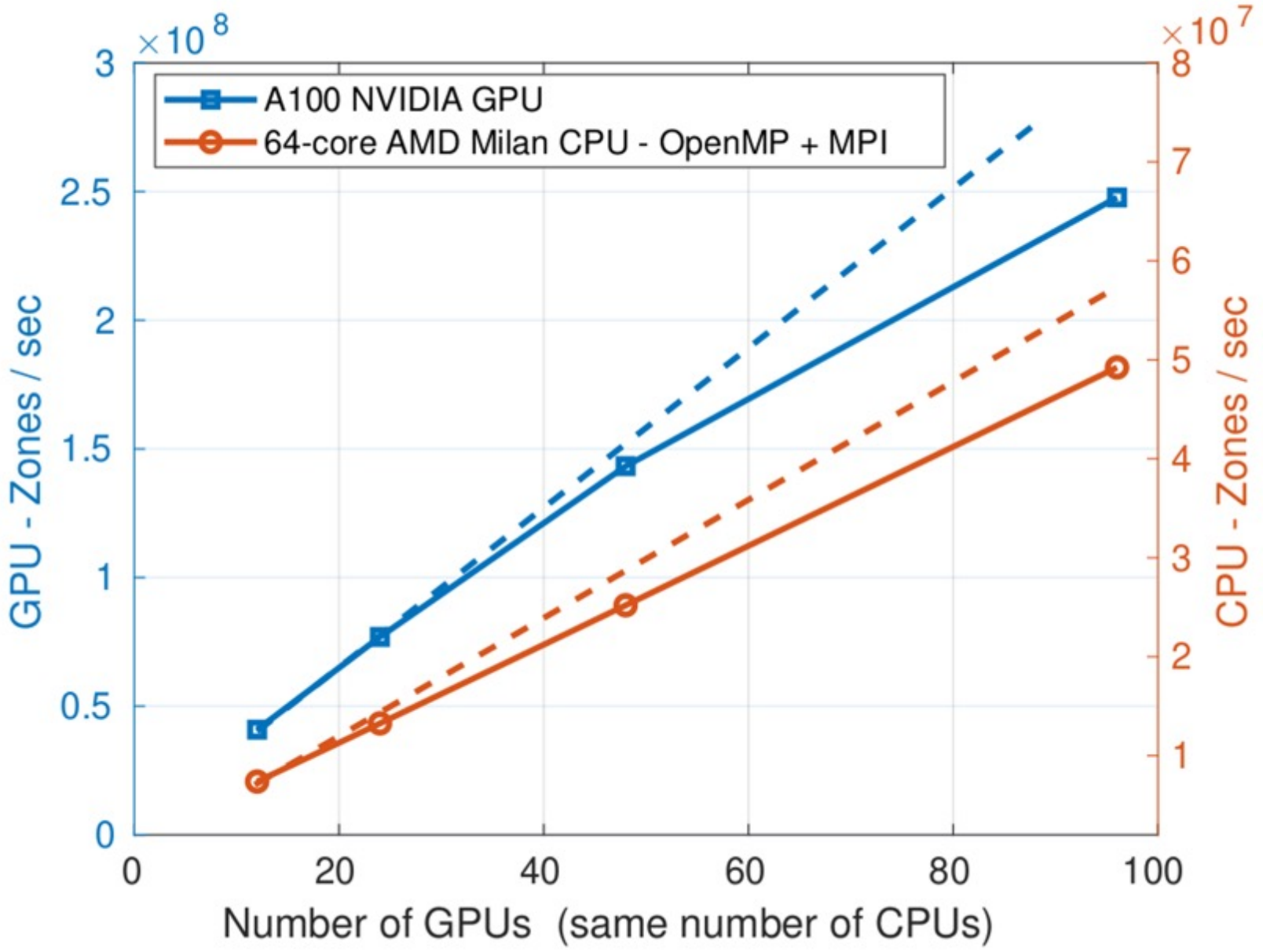

GPU performance:

- Code optimized for Nvidia A100 cache memory.
- 1 A100 GPU outperforms 5 AMD Milan CPUs
- Typical 4×A100 node outperforms ten 2×AMD Milan CPU nodes.
- Simulations performed at Notre Dame CRC and NCSA Delta GPU clusters.

Resonance Line Scattering

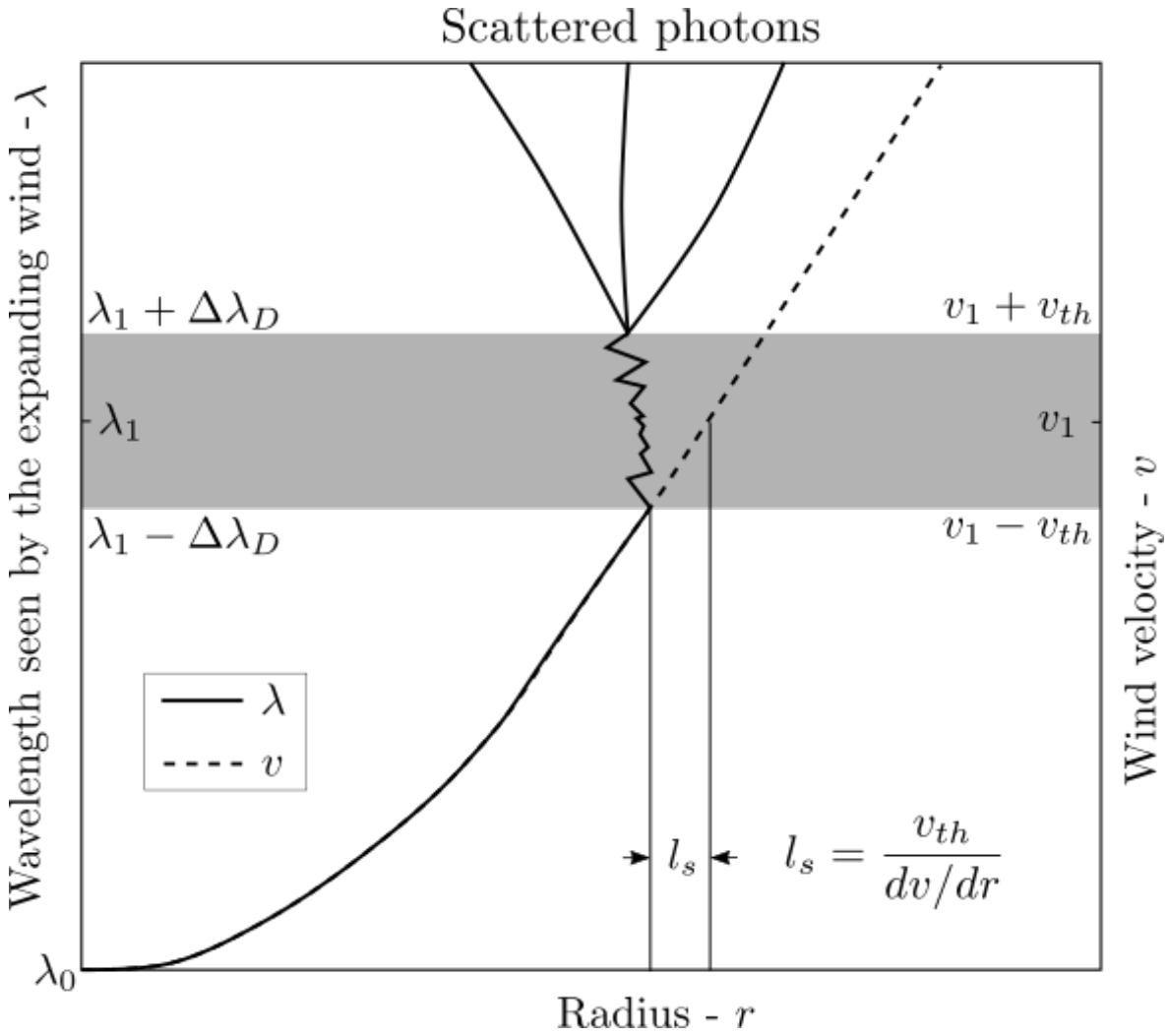

- The radiation force due to resonant absorption could be 1000x more than the gravitational pull
- This is not a continuous force.
- The doppler shifting of the accelerated mass keeps the resonant line force, a continuous force
- Figure – Journey of one photon (λ_0):
  - Line resonance as seen by the accelerating moving wind with photon (λ_0)
  - Wavelength starts red shifting as the wind velocity rises
  - Shaded region: Red shifted photon comes within the resonant band of the moving wind